Direct backward third-harmonic generation in nanostructures

Chieh-Feng Chang,[1] Hsing-Chao Chen,[2] Miin-Jang Chen,[2] Wei-Rein Liu,[3] Wen-Feng Hsieh,[3] Chia-Hung Hsu,[3,4] Chao-Yu Chen,[5] Fu-Hsiung Chang,[5] Che-Hang Yu,[1] and Chi-Kuang Sun[1,6]*

[1]*Department of Electrical Engineering and Graduate Institute of Photonics and Optoelectronics, National Taiwan University, Taipei 10617, Taiwan*
[2]*Department of Material Science and Engineering, National Taiwan University, Taipei 10617, Taiwan*
[3]*Department of Photonics and Institute of Photonics and Institute of Electro-Optical Engineering, National Chiao Tung University, Hsinchu 300, Taiwan*
[4]*National Synchrotron Radiation Research Center, Hsinchu 300, Taiwan*
[5]*Graduate Institute of Biochemistry and Molecular Biology, National Taiwan University, Taipei 100, Taiwan*
[6]*Research Center for Applied Sciences, Academia Sinica, Taipei 11529, Taiwan*
*[*sun@cc.ee.ntu.edu.tw](mailto:sun@cc.ee.ntu.edu.tw)*

Abstract: Direct-backward third harmonic generation (DBTHG) has been regarded as negligible or even inexistent due to the large value of wave-vector mismatch. In the past, BTHG signals were often interpreted as back-reflected or back-scattered forward-THG (FTHG). In this paper, we theoretically and experimentally demonstrate that backward third harmonic waves can be directly generated, and that their magnitude can be comparable with FTHG in nanostructures. Experimental data of DBTHG from ZnO thin films, CdSe quantum dots and Fe_3O_4 nanoparticles agree well with simulation results based on the Green's function. An integral equation was also derived for fast computation of DBTHG in nano films. Our investigation suggests that DBTHG can be a potentially powerful tool in nano-science research, especially when combined with FTHG measurements.

©2010 Optical Society of America

OCIS codes: (190.4160) Multiharmonic generation; (310.6628) Subwavelength structures, nanostructures

References and links

1. S.-Y. Chen, C.-S. Hsieh, S.-W. Chu, C.-Y. Lin, C.-Y. Ko, Y.-C. Chen, H.-J. Tsai, C.-H. Hu, and C.-K. Sun, "Noninvasive harmonics optical microscopy for long-term observation of embryonic nervous system development *in vivo*," J. Biomed. Opt. **11**(5), 054022 (2006).
2. S.-Y. Chen, H.-C. Yu, I.-J. Wang, and C.-K. Sun, "Infrared-based third and second harmonic generation imaging of cornea," J. Biomed. Opt. **14**(4), 044012 (2009).
3. C.-S. Hsieh, C.-Y. Ko, S.-Y. Chen, T.-M. Liu, J.-S. Wu, C.-H. Hu, and C.-K. Sun, "*In vivo* long-term continuous observation of gene expression in zebrafish embryo nerve systems by using harmonic generation microscopy and morphant technology," J. Biomed. Opt. **13**(6), 064041 (2008).
4. C.-K. Sun, C.-H. Yu, S.-P. Tai, C.-T. Kung, I.-J. Wang, H.-C. Yu, H.-J. Huang, W.-J. Lee, and Y.-F. Chan, "*In vivo* and *ex vivo* imaging of intra-tissue elastic fibers using third-harmonic-generation microscopy," Opt. Express **15**(18), 11167–11177 (2007).
5. D. Débarre, W. Supatto, A.-M. Pena, A. Fabre, T. Tordjmann, L. Combettes, M.-C. Schanne-Klein, and E. Beaurepaire, "Imaging lipid bodies in cells and tissues using third-harmonic generation microscopy," Nat. Methods **3**(1), 47–53 (2006).
6. D. Yelin, and Y. Silberberg, "Laser scanning third-harmonic-generation microscopy in biology," Opt. Express **5**(8), 169–175 (1999).
7. S.-W. Chu, I.-H. Chen, T.-M. Liu, C.-K. Sun, S.-P. Lee, B.-L. Lin, P.-C. Cheng, M.-X. Kuo, D.-J. Lin, and H.-L. Liu, "Nonlinear bio-photonic crystal effects revealed with multimodal nonlinear microscopy," J. Microsc. **208**(3), 190–200 (2002).
8. C.-S. Hsieh, S.-U. Chen, Y.-W. Lee, Y.-S. Yang, and C.-K. Sun, "Higher harmonic generation microscopy of *in vitro* cultured mammal oocytes and embryos," Opt. Express **16**(15), 11574–11588 (2008).
9. S.-W. Chu, S.-Y. Chen, T.-H. Tsai, T.-M. Liu, C.-Y. Lin, H.-J. Tsai, and C.-K. Sun, "*In vivo* developmental biology study using noninvasive multi-harmonic generation microscopy," Opt. Express **11**(23), 3093–3099 (2003).

10. S.-P. Tai, Y. Wu, D.-B. Shieh, L.-J. Chen, K.-J. Lin, C.-H. Yu, S.-W. Chu, C.-H. Chang, X.-Y. Shi, Y.-C. Wen, K.-H. Lin, T.-M. Liu, and C.-K. Sun, "Molecular imaging of cancer cells using plasmon-resonant-enhanced third-harmonic-generation in silver nanoparticles," Adv. Mater. **19**(24), 4520–4523 (2007).
11. J.-H. Lee, S.-Y. Chen, C.-H. Yu, S.-W. Chu, L.-F. Wang, C.-K. Sun, and B.-L. Chiang, "Noninvasive *in vitro* and *in vivo* assessment of epidermal hyperkeratosis and dermal fibrosis in atopic dermatitis," J. Biomed. Opt. **14**(1), 014008 (2009).
12. I.-H. Chen, S.-W. Chu, C.-K. Sun, P.-C. Cheng, and B.-L. Lin, "Wavelength dependent damage in biological multi-photon confocal microscopy: a micro-spectroscopic comparison between femtosecond Ti: sapphire and Cr: forsterite laser sources," Opt. Quantum Electron. **34**(12), 1251–1266 (2002).
13. D. Yelin, Y. Silberberg, Y. Barad, and J. S. Patel, "Depth-resolved imaging of nematic liquid crystals by third-harmonic microscopy," Appl. Phys. Lett. **74**(21), 3107 (1999).
14. V. I. Shcheslavskiy, S. M. Saltiel, A. R. Faustov, G. I. Petrov, and V. V. Yakovlev, "How to measure $\chi^{(3)}$ of a nanoparticle," Opt. Lett. **31**(10), 1486–1488 (2006).
15. J. A. Squier, and M. Müller, "Third-harmonic generation imaging of laser-induced breakdown in glass," Appl. Opt. **38**(27), 5789–5794 (1999).
16. C.-K. Sun, S.-W. Chu, S.-P. Tai, S. Keller, U. K. Mishra, and S. P. DenBaars, "Scanning second-harmonic/third-harmonic generation microscopy of gallium nitride," Appl. Phys. Lett. **77**(15), 2331 (2000).
17. S.-W. Chu, M.-C. Chan, S.-P. Tai, S. Keller, S. P. DenBaars, and C.-K. Sun, "Simultaneous four-photon luminescence, third-harmonic generation, and second-harmonic generation microscopy of GaN," Opt. Lett. **30**(18), 2463–2465 (2005).
18. C.-K. Sun, S.-W. Chu, S.-Y. Chen, T.-H. Tsai, T.-M. Liu, C.-Y. Lin, and H.-J. Tsai, "Higher harmonic generation microscopy for developmental biology," J. Struct. Biol. **147**(1), 19–30 (2004).
19. L. Canioni, S. Rivet, L. Sarger, R. Barille, P. Vacher, and P. Voisin, "Imaging of Ca$^{(2)+}$ intracellular dynamics with a third-harmonic generation microscope," Opt. Lett. **26**(8), 515–517 (2001).
20. C.-K. Sun, C.-C. Chen, S.-W. Chu, T.-H. Tsai, Y.-C. Chen, and B.-L. Lin, "Multiharmonic-generation biopsy of skin," Opt. Lett. **28**(24), 2488–2490 (2003).
21. T.-H. Tsai, S.-P. Tai, W.-J. Lee, H.-Y. Huang, Y.-H. Liao, and C.-K. Sun, "Optical signal degradation study in fixed human skin using confocal microscopy and higher-harmonic optical microscopy," Opt. Express **14**(2), 749–758 (2006).
22. V. Barzda, C. Greenhalgh, J. Aus der Au, S. Elmore, J. van Beek, and J. Squier, "Visualization of mitochondria in cardiomyocytes by simultaneous harmonic generation and fluorescence microscopy," Opt. Express **13**(20), 8263–8276 (2005).
23. S.-P. Tai, T.-H. Tsai, W.-J. Lee, D.-B. Shieh, Y.-H. Liao, H.-Y. Huang, K. Zhang, H.-L. Liu, and C.-K. Sun, "Optical biopsy of fixed human skin with backward-collected optical harmonics signals," Opt. Express **13**(20), 8231–8242 (2005).
24. S.-Y. Chen, S.-P. Tai, T.-H. Tsai, and C.-K. Sun, "Direct backward-emitted third-harmonic generation and its application to clinical microscopy," in *Quantum Electronics and Laser Science Conference, 2005. QELS '05*(2005), p. 167.
25. S.-P. Tai, W.-J. Lee, D.-B. Shieh, P.-C. Wu, H.-Y. Huang, C.-H. Yu, and C.-K. Sun, "*In vivo* optical biopsy of hamster oral cavity with epi-third-harmonic-generation microscopy," Opt. Express **14**(13), 6178–6187 (2006).
26. D. Débarre, N. Olivier, and E. Beaurepaire, "Signal epidetection in third-harmonic generation microscopy of turbid media," Opt. Express **15**(14), 8913–8924 (2007).
27. S.-Y. Chen, C.-Y. S. Hsu, and C.-K. Sun, "Epi-third and second harmonic generation microscopic imaging of abnormal enamel," Opt. Express **16**(15), 11670–11679 (2008).
28. S.-Y. Chen, H.-Y. Wu, and C.-K. Sun, "*In vivo* harmonic generation biopsy of human skin," J. Biomed. Opt. **14**(6), 060505 (2009).
29. J. X. Cheng, and X. S. Xie, "Green's function formulation for third-harmonic generation microscopy," J. Opt. Soc. Am. B **19**(7), 1604–1610 (2002).
30. R. W. Boyd, *Nonlinear optics* (Academic Press, Amsterdam; Boston, 2003).
31. J. M. Schins, T. Schrama, J. Squier, G. J. Brakenhoff, and M. Muller, "Determination of material properties by use of third-harmonic generation microscopy," J. Opt. Soc. Am. B **19**(7), 1627–1634 (2002).
32. U. Ozgur, Y. I. Alivov, C. Liu, A. Teke, M. A. Reshchikov, S. Dogan, V. Avrutin, S. J. Cho, and H. Morkoc, "A comprehensive review of ZnO materials and devices," J. Appl. Phys. **98**, 103 (2005).
33. J. T. Seo, S. M. Ma, Q. Yang, L. Creekmore, R. Battle, H. Brown, A. Jackson, T. Skyles, B. Tabibi, W. Yu, S. S. Jung, and M. Namkung, "Large Resonant Third-order Optical Nonlinearity of CdSe Nanocrystal Quantum Dots," J Phys. Conf. Ser. **38**, 91–94 (2006).
34. M. J. Weber, *Handbook of Optical Materials* (CRC Press, 2003).
35. V. I. Shcheslavskiy, S. M. Saltiel, A. Faustov, G. I. Petrov, and V. V. Yakovlev, "Third-harmonic Rayleigh scattering: theory and experiment," J. Opt. Soc. Am. B **22**(11), 2402–2408 (2005).
36. Y. Segawa, C. Y. Liu, B. P. Zhang, and N. T. Binh, "Third-harmonic generation from ZnO films deposited by MOCVD," Appl. Phys. B **79**(1), 83–86 (2004).
37. J. Miragliotta, and D. Wickenden, "Optical third-harmonic studies of the dispersion in χ(3) for gallium nitride thin films on sapphire," Phys. Rev. B **50**(20), 14960–14964 (1994).
38. H.-C. Chen, M.-J. Chen, M.-K. Wu, Y.-C. Cheng, and F.-Y. Tsai, "Low-threshold stimulated emission in ZnO thin films grown by atomic layer deposition," IEEE J. Sel. Top. Quantum Electron. **14**(4), 1053–1057 (2008).
39. W. R. Liu, W. F. Hsieh, C. H. Hsu, K. S. Liang, and F. S. S. Chien, "Threading dislocations in domain-matching epitaxial films of ZnO," J. Appl. Cryst. **40**(5), 924–930 (2007).

40. M. Bass, E. W. Van Stryland, D. R. Williams, and W. L. Wolfe, *Handbook of optics. Vol. 2, Devices, measurements, and properties* (McGraw-Hill New York, USA, 1995).
41. C.-F. Chang, C.-Y. Chen, F.-H. Chang, S.-P. Tai, C. Y. Chen, C. H. Yu, Y. B. Tseng, T. H. Tsai, I. S. Liu, W. F. Su, and C. K. Sun, "Cell tracking and detection of molecular expression in live cells using lipid-enclosed CdSe quantum dots as contrast agents for epi-third harmonic generation microscopy," Opt. Express **16**(13), 9534–9548 (2008).
42. C.-Y. Chen, C.-K. Sun, S.-P. Tai, C.-F. Chang, S.-H. Wu, Y. Hung, C.-Y. Mou, L.-W. Hsin, C.-Y. Cheng, J.-H. Chen, and F.-H. Chang are preparing a manuscript to be called "Clinically-Approved Magnetic Nanoparticles for High Resolution Optical Molecular Imaging Using Third Harmonic Generation."
43. T. Hashimoto, T. Yamada, and T. Yoko, "Third-order nonlinear optical properties of sol–gel derived α-Fe_2O_3, γ-Fe_2O_3, and Fe_3O_4 thin films," J. Appl. Phys. **80**(6), 3184 (1996).

1. Introduction

Third-harmonic generation (THG) is an electric-dipole-allowed process and is therefore non-vanishing in all materials, regardless of being centrosymmetric or not. Because of the Gouy phase shift, THG signals from a focused Gaussian beam can be observed only in the vicinity of interfaces, where the first- or the third-order susceptibilities are not homogeneous. This interface-sensitive feature makes THG a versatile tool in biological applications [1–12] and material science studies [13–17]. Due to momentum conservation, most of the third-harmonic waves are generated in the forward direction, and previous experimental setups were largely limited to the transmission-type geometry [5–7,18–22]. In many applications, however, collection of backward THG (BTHG) would be the only option, such as microscopy on optically-thick or highly-scattering samples. In other cases where a transmission-type configuration is possible, detection of BTHG would provide additional information when combined with signals from forward THG (FTHG) [23]. An understanding on the behaviors of BTHG is thus essential and deserves special attention.

Applications of BTHG have been successfully demonstrated in previous years, such as microscopy *ex vivo* or *in vivo* [23–28]. The origin of such signals, however, remains controversial. Many people assert that there should be no directly-generated BTHG (DBTHG) because of the large value of wave-vector mismatch. Instead, they believe these signals should come from back-reflected or back-scattered FTHG. In this paper, we demonstrate that DBTHG can be of comparable signal strength as FTHG in nanostructures. Using the Green's function for theory and simulation, we show that the ratio of DBTHG/FTHG is a strong function of material dimension in thin films and nanoparticles, both of which are important structures in nanosciences. An integral equation was also derived from wave equations for fast computation of BTHG from thin film structures. Experiments were performed on ZnO thin films, CdSe quantum dots and Fe_3O_4 nanoparticles, and the data agree well with the simulation results. Our research indicates that DBTHG plays an important role in nanostructures and can potentially reveal more information than FTHG.

2. Theory and Simulation

2.1 Calculation of THG with the Green's function

The dyadic Green's function was used to calculate the THG strength both in the direct-backward- and the forward-directions [29]:

$$\mathbf{E}^{(3\omega)}(\mathbf{R}) \propto \iiint_V dV \left(\overline{\mathbf{I}} + \frac{\nabla\nabla}{k_3^2} \right) \frac{\exp\left(ik_3|\mathbf{R}-\mathbf{r}|\right)}{|\mathbf{R}-\mathbf{r}|} \cdot \mathbf{P}^{(3\omega)}(\mathbf{r}), \tag{1}$$

$$P^{(3\omega)} \propto \int_\theta d\theta \int_0^{2\pi} d\phi \left| \mathbf{E}^{(3\omega)}(\mathbf{R}) \right|^2 R^2 \sin\theta. \tag{2}$$

Here, $\mathbf{R}$ and $\mathbf{r}$ are coordinates of observation and source points, respectively, $\overline{\mathbf{I}}$ is the idemfactor, ∇ is the dyadic del operator, k_3 is the wave-vector amplitude at 3ω in the matrix, and $\mathbf{P}^{(3\omega)}(\mathbf{r})$ is the laser-induced third-order polarization inside the sample structure. To calculate $\mathbf{P}^{(3\omega)}(\mathbf{r})$, the excitation field was modeled as a focused Gaussian beam. The refractive indices of sample materials were calculated with associated Sellmeier equations, both at 3ω to

calculate $k_3 = n_3 \cdot 2\pi / \lambda$ and at ω to determine the material-dependent optical distance z inside the sample structure.

2.2 Integral equation for thin film structures

While the generality of the Green's function enables it to deal with arbitrary sample shapes and various descriptions of focused laser beams, this feature also means heavy consumption of computation resources and the absence of an insightful prediction of calculation results. An easy and powerful method is thus required to effectively interpret DBTHG data in further details. In particular, thin films are commonly encountered in experiments, for example cell membranes in tissues and epitaxial layers in semiconductors. Such an approach for investigating thin films would then be valuable in the context of both qualitative and quantitative measurements. Here we propose a simple yet effective method to calculate DBTHG in layered structures. Using the paraxial wave equation, the approach is straightforward, physically intuitive and computationally economical.

Consider a focused Gaussian beam propagating in the $+z$ direction; the electric field of the fundamental wave can be expressed as [30]

$$E = \frac{A_\omega}{(1+i\zeta)} \exp\left(-\frac{r^2}{w_0^2(1+i\zeta)}\right) \exp(ik_1 z - i\omega t) + c.c., \qquad (3)$$

where A_ω is a constant, w_0 is the beam waist of the fundamental Gaussian beam, $\zeta = z / b$, and $b = k_1 w_0^2 / 2 = \pi n_1 w_0^2 / \lambda_1$ is the confocal parameter. Following similar procedures as those of Boyd [30], the FTHG equation can be derived as

$$A_{\mathrm{FTHG},3\omega} = i\frac{3\omega}{8c} A_\omega^3 \int_{-\infty}^{z} \frac{\chi^{(3)}}{n_3} \frac{1}{(1+i\zeta')^2} \exp\left(i(3k_1 - k_3)z'\right) dz'. \qquad (4)$$

The nonlinear wave equation for a backward-propagating wave $E_{3\omega}\exp(-ik_3 z - i\omega t)$ can be written, in SI units, as [30]

$$\left[\frac{1}{2ik_3}\nabla_T^2 - \frac{\partial}{\partial z}\right] E_{3\omega} = i\frac{3\omega}{8n_3 c}\chi^{(3)}\frac{A_\omega^3}{(1+i\zeta)^3}\exp\left(-\frac{3r^2}{w_0^2(1+i\zeta)}\right)\exp(i\Delta kz), \qquad (5)$$

where $\Delta k = 3k_1 + k_3$ is the phase mismatch between the excitation field and the backward-emitting, third-order nonlinear polarization. Since the DBTHG wave should also be a Gaussian beam, we adopted the trial solution of

$$E_{3\omega} = \frac{A_{\mathrm{BTHG},3\omega}}{(1-i\zeta)}\exp\left(-\frac{3r^2}{w_0^2(1-i\zeta)}\right). \qquad (6)$$

Now that THG is only significant around the beam waist, and that we are considering nano thin films that only extend to a small fraction of a wavelength in the z direction, we imposed an approximation of quasi-planar wave front and neglected the curvature of wave fronts in the equation. In Eqs. (5) and 6, $1 \pm i\zeta$ in the exponential terms (radial field profiles) were discarded, but $1 \pm i\zeta$ in the longitudinal terms were kept since they represent the important information of Gouy phase shift across the beam waist. The equation can then be solved as

$$A_{\mathrm{BTHG},3\omega} = i\frac{3\omega}{8c}A_\omega^3 \int_{z}^{\infty}\frac{\chi^{(3)}}{n_3}\left(\frac{1-i\zeta'}{(1+i\zeta')^3}\right)\exp\left(i(3k_1 + k_3)z'\right) dz'. \qquad (7)$$

In reality, a nanometer-scale thin film rarely appears isolated in air or vacuum, and when it is attached to or sandwiched between other media, the equations for THG have to be modified accordingly. Following similar approaches of Schins *et al.* [31], we consider the following two conditions when an interface is crossed. For one thing, the q-parameter, or more

specifically the medium-dependent optical distance to the focal plane, is changed because the laser beam enters a region with a different refractive index. For the other, the phase difference is maintained constant between the generated third-harmonic wave and the material third-order polarization, and a phase correction term is introduced at each interface. Equation (7) is then modified as

$$A_{BTHG,3\omega} = i\frac{3\omega}{8c}A_\omega^3 \sum_j \exp(i\Delta\phi_j)\int_{q_j}^{r_j} \frac{\chi_j^{(3)}}{n_{3,j}}\frac{1-i\zeta'}{(1+i\zeta')^3}\exp(i\Delta k_j z')dz', \tag{8}$$

where j denotes each region and the following terms are calculated iteratively:

$r_j - q_j$ = layer thickness,

$$\frac{q_{j+1}}{n_{1,j+1}} = \frac{r_j}{n_{1,j}},$$

$$\Delta\phi_{j+1} - \Delta\phi_j = \Delta k_j r_j - \Delta k_{j+1} q_{j+1}.$$

2.3 Simulation results of THG from nano thin films

First we consider an isolated thin film in air, as depicted in Fig. 1(a). The laser beam was supposed to focus on the surface of the thin film, which is modeled as ZnO for further comparison with the results in the experimental section. The refractive indices were calculated to be n_1 = 1.934 at 1230 nm and n_3 = 2.229 at 410 nm, according to the Sellmeier equation [32]. The observation cone angle was defined as θ = 157° to 180° and 0° to 33° for BTHG and FTHG, respectively, corresponding to the numerical aperture (NA) 0.55 aspheric lens used in the experiment. All calculated values are normalized to the maximum of FTHG strength. Figures 1(b) and 1(c) show the calculated results of FTHG and BTHG, respectively, as a function of film thickness. While the FTHG amplitude is well known to be monotonically increasing, the DBTHG trace is heavily oscillatory due to the large phase mismatch Δk, which mainly determines the period between peaks. The ratio of BTHG/FTHG is then plotted in Fig. 1(d). As the film grows thicker, the BTHG intensity is much weaker than FTHG because the large phase mismatch introduces significant destructive interference and impedes the buildup of signal strength. This is the traditional regime of bulk optics or micro-photonics, where effects of constructive and destructive interference make FTHG much stronger than DBTHG. In this regime, DBTHG is typically ignored or confused with back-scattered FTHG. It should be noted, however, that this ratio increases rapidly when the film thickness becomes thinner; eventually the ratio reaches unity as the thickness approaches zero. This is intuitively correct because in this extreme case, the excitation polarization becomes a sheet of element dipoles, whose far-field radiation patterns are supposed to be symmetric in both the epi- and forward directions. It should be also noted that the simulations results from the Green's function and from the integral equation are very similar to each other, which validates the assumptions made during the derivation of the simplified equation.
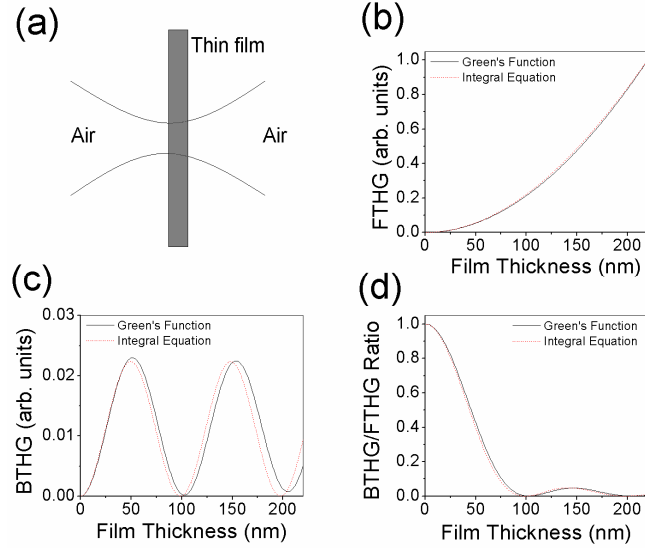
Fig. 1. Numerical simulations of THG strength as a function of ZnO thin film thickness. (a) The focusing geometry for the simulation. The focal plane is set on the surface of thin films. (b) FTHG strength, normalized to its maximum. (c) BTHG strength, normalized to the maximum of FTHG. (d) The ratio between backward and forward THG. Black solid and red dashed lines represent the simulation results using the Green's function and the integral equation, respectively.

2.4 Simulation results of THG from nanospheres

Next we consider an isolated nanosphere placed at the center of the beam waist. Again, for future comparison we model the nanosphere as a CdSe quantum dot in aqueous solution. Because the $\chi^{(3)}$ value of CdSe is much larger than that of water [33], it can be regarded as an isolated sphere and the volume of integration V was limited to the particle region. The refractive index of CdSe at 1230 nm was calculated to be 2.523 [34]. For $k_3 = n_3 \cdot 2\pi / \lambda$, $n_3 =$ 1.344 is the refractive index of water in this case [34]. Because the particle size was much smaller than the wavelength, diffraction at the particle-solvent interface was ignored in our calculation. The observation cone angle was defined as $\theta = 115°$ to $180°$ and $0°$ to $65°$ for BTHG and FTHG calculations, respectively, corresponding to the NA 1.2 objective used in the experiment. The value was calculated by $\alpha = \sin^{-1} (NA/n_1) = 65°$, where n_1 is the refractive index at ω in the matrix [29] and is chosen to be 1.325 for water here [34]. Again the calculated values are normalized to the maximum of FTHG strength. The values of FTHG, BTHG and BTHG/FTHG ratio are then plotted in Figs. 2(a), 2(b) and 2(c), respectively.

When Figs. 2(b) and 1(c) are compared, it can be observed that size-dependent BTHG amplitudes from nanoparticles and nano films exhibit rather different trends, which can be interpreted with a relatively simple and straightforward picture. Since a focused Gaussian beam was used for simulation, the beam profile would be symmetric to the z-axis, the direction of beam propagation. Referring to Fig. 2(d), we can consider the laser beam as a collection of concentric, cylindrical layers infinite in number. Each cylindrical layer would change its amplitude and phase along the z-direction, and each layer can be further decomposed as a set of infinite rays. We now can follow a similar procedure as in [35] to predict the behaviors of BTHG. The strength of BTHG can then be expressed as

$$I_{BTHG} \propto \int_0^r \rho \, g^2(\rho) \left| \int_{z_1}^{z_2} F(\rho, z) dz \right|^2 d\rho \tag{9}$$

where r is the radius of the nanosphere, $g(\rho)$ is a function of the Gaussian beam radial distribution, $F(\rho,z)$ represents some interaction function of each ray in the sphere, and $z_{1,2}$ denotes the interaction length of each ray in the sphere. Since the integrand is equal to or larger than zero, $\left|\int_{z_1}^{z_2} F(\rho,z)dz\right|$ has to be close to zero for there to be almost no backward THG.

For a thin film structure $z_{1,2}$ are the same for each cylindrical layer, and it is possible that nearly total destructive interference is achieved so that BTHG is ~0 at a certain thickness. In a sphere, however, $z_{1,2}$ changes continuously as ρ changes from 0 to r, the generated THG intensity has to be almost zero in all conditions for BTHG to be ~0. Since this does not sound physically intuitive, BTHG from nanoparticles are not supposed to drop to ~0 at certain diameters, which agrees with the simulation results. Furthermore, while the cross section of THG interaction remains fixed in thin films, in nanospheres the cross section becomes larger as the particle size increases. As a result, the BTHG strength shows a generally increasing trend as a function of particle size. This is in sharp contrast with Fig. 1(c), in which the values local maxima and minima remain approximately the same over the simulated range of thickness.
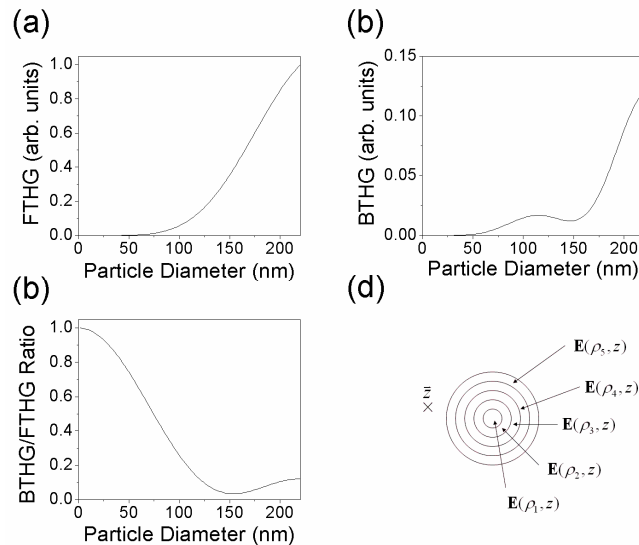
(a)

(b)

(b)

(d)

Fig. 2. Numerical simulations of THG strength from CdSe quantum dots, plotted as a function of particle diameter. (a) FTHG strength, normalized to its maximum. (b) BTHG strength, normalized to the FTHG maximum. (c) BTHG/FTHG ratio. (d) Schematics of a Gaussian beam for BTHG interpretation. A Guassian beam can be interpreted as a collection of concentric, cylindrical layers infinite in number, each of which in turn can be further decomposed as a set of infinite rays.

3. Experimental Results and Discussion

To corroborate the aforementioned theory and simulation, we conducted experiments of FTHG and BTHG on ZnO thin films, CdSe quantum dots and Fe_3O_4 nanoparticles. Since isolated nano films are difficult for synthesis and manipulation, we designed the sample structure to be ZnO thin films deposited on sapphire. Because the $\chi^{(3)}$ value of nanofilm ZnO ($\sim 3.77\times10^{-12}$ esu [36],) is much larger than that of sapphire (1.15×10^{-14} esu [37],), we expected the THG response of such samples should be close to isolated films. These thin films were grown on c-plane sapphire substrates by either atomic layer deposition (ALD) [38] or pulsed-laser deposition (PLD) [39]. Five groups of samples were used in this experiment and the thicknesses were determined by scanning electron microscopy (SEM) to be 45, 73, 113, 163 and 200 nm, respectively. The excitation source was an optical parametric oscillator (Mira-

OPO, Coherent, U.S.A.) synchronously pumped by a Ti:sapphire laser (Mira Optima 900-F, Coherent, U.S.A.), and the wavelength was locked at 1230 nm. Figure 3 shows the schematics of the experimental setup; Fig. 3(a) is the configuration for BTHG and FTHG measurements, and Fig. 3(b) is for calibration procedures. In our setup, two identical aspheric lenses (C230TM-C, NA = 0.55, Thorlabs, U.S.A.) were used for illumination and collection so that the relative strength of BTHG and FTHG can be quantitatively calibrated. First, a piece of sapphire substrate was z-scanned as in Fig. 3(a) to obtain the position-dependent trace of FTHG. The experimental setup was then switched to Fig. 3(b), and the half-wave plate was rotated accordingly so that the laser power before the illumination lens remained the same. The FTHG z-scan was performed again in this configuration. Let s_1 and s_2 be the measured FTHG strength when the laser beam is focused on the interface closer to the illumination lens in Figs. 3(a) and 3(b), respectively. Since the illumination-collection set was symmetric, these two values represented the same signal level and their difference accounts for other factors of dissymmetry, such as different PMT sensitivities and different degrees of misalignment between the collection lens and the PMT in these two arms. Suppose for the configuration 3(a) the raw signals of FTHG and BTHG were measured to be f_0 and b_0, respectively. The BTHG/FTHG ratio can then be calculated as BTHG: FTHG = (b_0 / s_2): (f_0 / s_1).
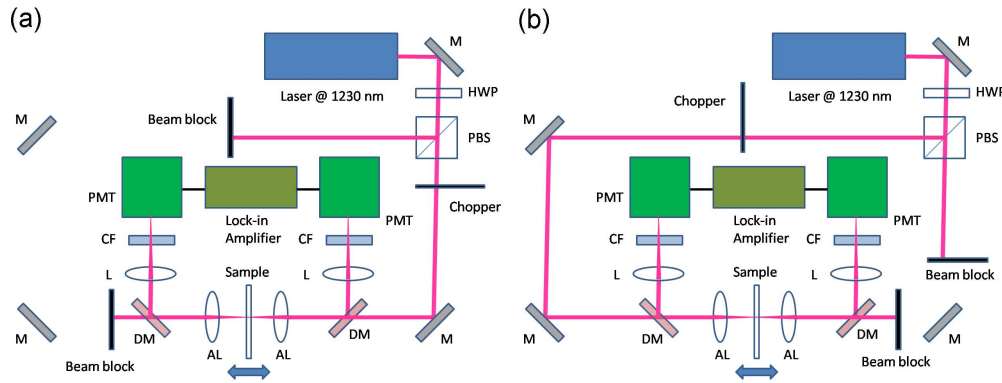

Fig. 3. Schematics of the experimental setup. (a) Configuration for BTHG and FTHG measurements. (b) Configuration for signal calibration. M: mirror; HWP: half-wave plate; PBS: polarization beam-splitter; DM: dichroic mirror; L: lens; CF: color filter; PMT: photomultiplier tube; AL: aspheric lens.

The ratio of BTHG/FTHG from experimental and simulation results are plotted in Fig. 4(a). To simulate the generation of third-harmonic waves in sapphire, $n_1 = 1.752$ and $n_3 = 1.785$ were calculated from its Sellmeier equation [40]. The final BTHG/FTHG ratios were calculated by incorporating surface reflection at the sapphire/air and the ZnO/air interfaces at 410 nm. Although a large number of factors were not considered in our simulation (etalon effect in thin film, possible deviation from normal incidence, inhomogeneity of ZnO $\chi^{(3)}$, etc.), the experimental data agreed well with the simulation trace from the Green's function or from the integral equation. Most importantly, when the film thickness is thin enough the ratio can significantly exceed the reflectivity value of the sapphire-air interface, which is 7.94% at 410 nm. Our results indicate that the collected BTHG signals were directly-generated backward THG, not back-reflected or back-scattered FTHG. As the film thickness becomes larger, the FTHG strength far exceeds the BTHG and the ratio would decrease greatly, as shown in the figure. The results also justified our choice of sample design, in which the large contrast of film and substrate $\chi^{(3)}$ values can simulate an isolated thin film. To illustrate on this point, Fig. 4(b) shows the simulation results in which the $\chi^{(3)}$ value of ZnO was set to 100X even larger. In Fig. 4(a), when the film thickness approaches zero the BTHG/FTHG ratio would drop rapidly, because in this case the sample resembles a piece of sapphire and the contribution from the substrate dominates. In Fig. 4(b), the THG response from such a sample would be closer to an isolated thin film like in Fig. 1(d), as expected.
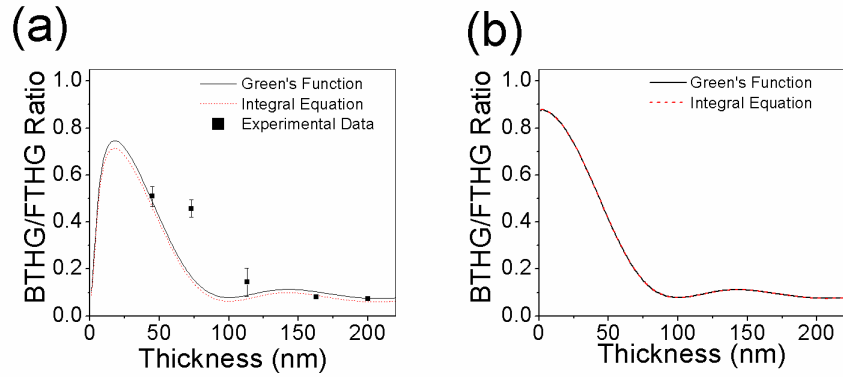
Fig. 4. (a) Experimental results of the BTHG/FTHG ratio from ZnO thin films on sapphire. The simulation trace is also plotted. (b) Simulation of the BTHG/FTHG ratio of ZnO thin films on sapphire, assuming the $\chi^{(3)}$ value of ZnO is increased by 100X. Black solid and red dashed lines represent the simulation results using the Green's function and the integral equation, respectively.

To investigate the BTHG behavior of nanospheres, CdSe lipid-enclosed quantum dots (LEQDs) and Fe_3O_4 LEQDs in aqueous solution were imaged by our epi-THG microscope. The excitation source was a home-built femtosecond Cr:forsterite laser centered at 1230 nm, with a 130 fs pulsewidth, a 110 MHz repetition rate and a 20 nm spectral full width at half maximum [23,25]. After being shaped by a telescope, the laser beam was directed into a modified beam-scanning system (Olympus FV300) and an upright microscope (Olympus BX51). A water-immersion objective (Olympus UplanApo/IR 60X/ NA 1.2/WD 0.2 mm) was used for illumination and collection. Full details of sample preparation, experimental configurations and data analysis can be found in our previous work [41,42]. The refractive index of Fe_3O_4 was calculated to be 2.059 at 1230 nm [43]; its $\chi^{(3)}$ value is also much larger than that of water [43], so the model of an isolated nanosphere still holds. The experimental and simulation results are then plotted in Fig. 5. The polydispersity of particles were also considered by further weighting the calculated curves with a Gaussian-shaped size distribution [41,42]:

$$P_{poly}^{(3\omega)}(d) \propto \int_{d'} dd' P^{(3\omega)}(d') \cdot \frac{1}{\sigma} \exp\left(-\frac{(d'-d)^2}{2\sigma^2}\right) \qquad (10)$$

The standard deviation is calculated by $\sigma = (d'/d_{ref}) \cdot \sigma_{ref}$, where the value of σ_{ref} is obtained from transmission electron microscopy (TEM) statistics. As can be seen in the figure, the experimental data fit well to the simulation on direct-epi-THG with polydispersity (solid lines) but deviate obviously from the trace of the FTHG (dashed lines), indicating that the signals we observed were indeed DBTHG, not FTHG back-scattered after generation.

It can be observed in both cases that due to the large phase mismatch between the excitation polarization and the generated wave, BTHG is much more sensitive to nano-scale variations of sample dimensions than FTHG. This feature may be potentially useful for nanophotonic investigation. If FTHG measurements are also feasible in an experiment, simultaneous retrieval of BTHG and FTHG signals can be used to calculate the BTHG/FTHG ratio, which can be a potentially powerful tool for quantitative analysis in the nano regime. With proper calibration of a microscopy system, for example, the BTHG image can be divided by the FTHG image pixel by pixel to generate a "ratio image," which can be juxtaposed with BTHG and FTHG images for further interpretation. Previously unavailable information, such as dimensions of cellular membranes or organelles in medical imaging, may be obtained in this approach.
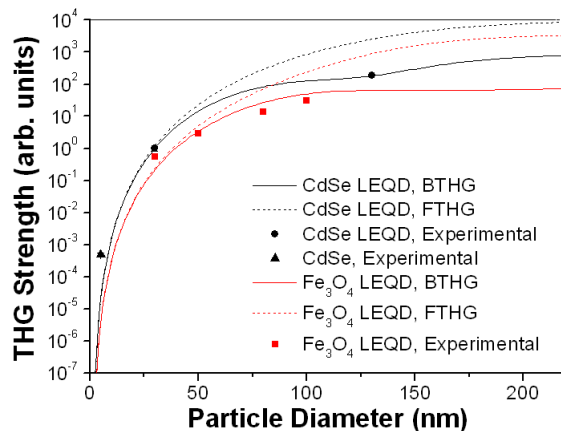
Fig. 5. Experimental results of BTHG in CdSe and Fe$_3$O$_4$ LEQDs. Solid and dashed lines represent simulation results of BTHG and FTHG, respectively, by assuming a Gaussian distribution of particle polydispersity. Results from CdSe and Fe$_3$O$_4$ calculations are plotted in black and red lines, respectively. Black circles, black triangles and red squares are measured THG signals from CdSe LEQDs, CdSe quantum dots and Fe$_3$O$_4$ LEQDs, respectively, in the epi-direction.

4. Conclusion

In summary, we demonstrated that backward THG can be directly generated and that its strength can be on the same order of FTHG in nanostructures. Using the Green's function as the theory, we performed numerical simulations on BTHG and FTHG in thin films and nanoparticles. We also derived an integral equation for BTHG calculation in nano films, which was shown to yield similar results to those from the Green's function. We experimentally investigated size-dependent BTHG from ZnO thin films on sapphire as well as CdSe quantum dots and Fe$_3$O$_4$ nanoparticles in aqueous solution, and the data agreed very well with the simulation results. Our research suggests that BTHG signals can potentially provide more information than FTHG in nanophotonic measurements, particularly when combined with FTHG signals to calculate the BTHG/FTHG ratios.

Acknowledgments